Photopyroelectric-quantum-yield spectroscopy and quantum-mechanical photoexcitation-decay kinetics of the Ti^{3+} ion in Al_2O_3

Marek Grinberg
Institute of Physics, Nicolaus Copernicus University, Torun 87-100, Poland

Andreas Mandelis
Photothermal and Optoelectronic Diagnostics Laboratory, Department of Mechanical Engineering, University of Toronto, Toronto, Canada M5S 1A4

(Received 6 December 1993)

Quadrature photopyroelectric spectra of the optical-to-thermal (nonradiative) energy conversion efficiency of Ti^{3+}:Al_2O_3 crystals were found to yield good agreement between the experimental quantum-yield spectrum of this optical material and detailed quantum-mechanical calculations of the nonradiative and radiative deexcitation kinetics of the Ti^{3+} ion in the Al_2O_3 host matrix. Both inter- and intraconfigurational decay mechanisms of the excited-state manifold were considered including fast nonradiative relaxations. The experimental quantum-yield spectra were found to be dominated by intraconfigurational nonradiative relaxation below the excited- and ground-electronic-state manifold crossover energy, E_{nr}; and by internal conversion processes in the highly vibronically excited Ti^{3+} ion above E_{nr}. A one-parameter fit of the quantum-yield model to the data gave the intraconfigurational relaxation time constant τ_{intra} for the Ti^{3+}:Al_2O_3 system. The present combined experimental and theoretical approach can be more generally applicable to other optoelectronic systems exhibiting strong electron-lattice coupling.

I. INTRODUCTION

The aim of this paper is the spectral acquisition and theoretical analysis of the quantum efficiency of fluorescence centers in solids and in Ti:sapphire in particular. We are interested in the dependence of the radiative and nonradiative deexcitation efficiency of the system on the energy of the exciting photons. Although we have performed detailed calculations for the Ti^{3+}:Al_2O_3 the results can be easily applied to transition-metal ions in other materials as well, in cases when strong electron-lattice coupling occurs.

The electronic structure of the octahedrally coordinated Ti^{3+} ion consists of the excited ^2E and the ground $^2T_2$ electronic manifolds.[1] The large Jahn-Teller $E^*\epsilon$ effect results in the relatively large probability of nonradiative internal conversion of the excited system directly to the highly excited vibronic states of the ground-electronic manifold.[2-4] These transitions are responsible for the decreases of the fluorescence decay time when the temperature increases.[2,5,6] Additional evidence for the crucial role of the strong electron-lattice coupling in the internal conversion process has been provided by investigations of the temperature dependence of the fluorescence decay time of the Ti^{3+} in other materials [e.g., in YAG (Ref. 7)] and also in other d^1 systems, such as V^{4+}.[8,9] In all these cases, a large Jahn-Teller effect and a rapid decrease of the fluorescence decay time and quantum efficiency with increasing temperature have been reported.

The strong coupling with the lattice results in crossover of the ground- and excited-electronic manifolds. One may consider these electronic manifolds as potential energies with a local minimum in the excited state and the global minimum in the ground state. Classically the nonradiative internal conversion from the excited to the ground-electronic manifold can take place when we excite the system above the crossing point. In the quantum-mechanical picture this probability is determined by the electronic transition moment and the overlap integrals of the vibronic wave functions related to the initial and final states. Thus the transition is probable even for energies smaller than the crossover point, while the transition probability for energies above the crossover energy is smaller than unity.

One distinguishes two competitive nonradiative processes: the above-mentioned internal conversion and the intraconfigurational relaxation. Since the probability for internal conversion increases by many orders of magnitude with increase of the initial state energy,[4] this process can be competitive with the relaxation inside the excited-electronic state and causes decrease of the quantum efficiency of highly excited systems.

This paper contains a theoretical treatment of the deexcitation kinetics of Ti:sapphire in order to analyze optical-to-thermal nonradiative energy conversion efficiency spectra obtained using quadrature photopyroelectric spectroscopy.[10,11] In Sec. II we describe the photopyroelectric experiments, which yielded the absorption and the nonradiative energy conversion efficiency spectra of the system. In Sec. III we consider the kinetics of deexcitation of a two-electronic manifold system, using the one-dimensional configuration coordinate space approximation. We also introduce definitions of the probabilities for intraconfigurational relaxation and internal

conversion, and calculate the quantum efficiency and nonradiative energy conversion efficiency of the system. In Secs. IV and V we further develop the theoretical model for the case of Ti:sapphire using a two-dimensional configurational coordinate scheme and apply the model to the analysis of the experimental nonradiative spectra of Ti:sapphire.

II. PHOTOPYROELECTRIC SPECTROSCOPY (PPES) OF Ti^{3+}:Al_2O_3 CRYSTALS. EXPERIMENTAL AND RESULTS

A. Optical absorptance, $\beta(\lambda)$.

The Ti:sapphire crystals used in this work were grown by the Czochralski pulling technique at Union Carbide, Washougal, WA. Details of the growth and post-growth processing have been given elsewhere.[11] The samples examined photopyroelectrically were two pairs of crystals with figure-of-merit (FOM) of 40 and 800, respectively. FOM is defined as the absorption ratio at 490 and 820 nm. Each pair included a long and a short crystal, both cut from the same rod. All four crystals were subjected to the same surface polish treatment. The reflectance spectra of the Ti:sapphire crystals were recorded, and these data were subsequently used in the analysis of the photopyroelectric spectra. Noncontact PPE spectra were obtained using a spectrometer, described elsewhere.[11] Optical transmission spectra were obtained from the in-phase (IP) -PPE lock-in signal in the purely optical mode. This signal is more than two orders of magnitude stronger than the quadrature (Q)-PPE (purely thermal-wave) mode.[11] The low level of signal exhibited by the Q-PPE mode is characteristic of very weakly absorbing optical materials and is equivalent to a phase shift in the 0.02°–0.2° range. As a result of the ultra small phase shifts detectable by the present noncontact spectrometer through the Q channel, the contribution of the thermally very efficient surface absorptions closest to the detector element may dominate bulk heating contributions in some spectral regions and thus the PPES signal requires deconvolution.[12] Normalized transmission data from each crystal pair (thicknesses l_1, l_2) taking into account the spectral throughput of the Xe lamp were used[12] along with reflectance spectra to obtain a system of two equations within two unknown parameters (β_b: bulk optical-absorption coefficient; A_s: surface absorptance) of the form

$$\beta_b l_1 + 2A_s = S_1 \ , \tag{1a}$$

$$\beta_b l_2 + 2A_s = S_2 \ . \tag{1b}$$

Equations (1a) and (1b) when solved for the spectral quantities $\beta_b(\lambda)l$ and $A_s(\lambda)$, yield deconvoluted bulk and surface absorptance spectra for both sets of samples.[12] The bulk absorptance for the FOM=40 sample pair is shown in Fig. 1 and is typical of the Ti^{3+}:Al_2O_3 system, consisting of a broad peak centered around 470 nm with a red-shifted shoulder. The peak is due to the $^2T_{2g} \rightarrow {}^2E_g$ transition broadened by phonons. The shoulder is the result of the Jahn-Teller splitting of the ^2E_g state.[6] Figure 1 also shows a similar spectrum for the FOM=800 pair

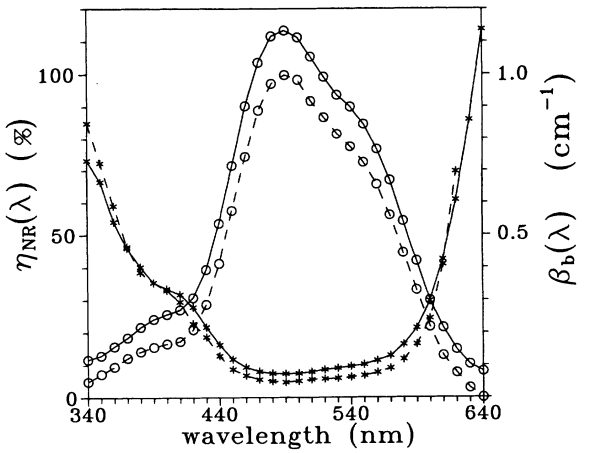

FIG. 1. Bulk optical-absorption coefficient (circles) and optical-to-thermal energy conversion (nonradiative) efficiency (asterisks) spectra of two pairs of Ti:sapphire crystal rods from Union Carbide, Washougal, WA. Solid curves correspond to FOM=40 samples; dashed curves correspond to FOM=800 samples.

of crystals. An important effect of the bulk/surface absorptance deconvolution is the observation that the bulk spectrum of the FOM=800 crystals becomes essentially zero below 640 nm and the surface absorption (not shown here) completely dominates the optical behavior of these materials.[12] For the FOM=40 crystals the overall bulk absorption is stronger than in the FOM=800 samples. This is probably due to the residual bulk absorption originating in crystal-growth defects.

The effects of surface absorptions, including the spectral regions dominated by them, have been fully discussed elsewhere.[12] In terms of bulk absorption coefficient spectra, the lower overall $\beta_b(\lambda)$ of the FOM=800 crystals is consistent with improved optical quality. This is the result of one additional annealing (in pure H_2 at 1940 °C for 180 h) of these crystals out of the original batch in which all our materials originated.[13] In Fig. 1 the bulk absorption cross section of the FOM=800 crystals becomes zero at ~640 nm, in agreement with the minimum photon energy threshold required to induce an $^2T_{2g} \rightarrow {}^2E_g$ electron transition [~6471 Å (Ref. 14)]. The near-IR bulk absorption of the FOM=40 ("unannealed") crystals is intrinsic to Czochralski-grown crystals and has been associated with Ti^{3+} ions in interstitial or defect sites close to native defects.[13] A different school of thought proposed that pairs of Ti^{3+}-Ti^{4+} ions are responsible,[6] based on observations of pair-related absorption in solutions.[15]

B. Optical-to-thermal bulk energy conversion efficiency, $\eta_{NR}^{(b)}(\lambda)$

Thermal energy generation spectra were recorded after the $L \rightarrow \infty$ (purely optical) measurements were performed, by decreasing the distance, L, between the sample surface and the pyroelectric detector to some predetermined value <1 mm, at which a measurable, stable and reproducible lock-in quadrature signal was

present. The quadratures of the PPES signals corresponding to "infinite" and finite L distances were subtracted at each wavelength. To ascertain that the PPE instrument was capable of producing realistic absolute $\eta_{NR}^{(b)}(\lambda)$ spectra, a test Si wafer sample was used, with a thin layer of soot on the polished surface facing the monochrometer. Under these conditions the PPE signal,[12] can be considerably simplified:

$$S_Q(\omega,\lambda)=\eta_{NR}^{(b)}(\lambda)F(\omega,l,L,\alpha_s,\gamma_{gs},\gamma_{gp}) , \quad (2)$$

where ω is the intensity modulation angular frequency of the exciting radiation, l is the sample thickness, L is the sample surface-to-pyroelectric detector distance, α_s is the sample thermal diffusivity, and γ_{gs}, γ_{gp} are thermal coupling coefficients between the surrounding gas (air;g) and the sample(s) or the pyroelectric element [polyvinylidene fluoride (PVDF); p]. F indicates a complicated functional dependence.[12]

For the sooted Si wafer η_{NR} is expected to be uniformly 100% throughout the entire spectral region of interest. Equation (2) was used to normalize the Q-PPES data and the $\eta_{NR}(\lambda)$ spectrum obtained quantitively is shown in Fig. 2. Curves from two successive experiments are shown, which indicate 100% ±3% variance in the reproducibility of the obtained η_{NR} values, with ±6% nonconstancy across the 380–650-nm range. These spectral variances were deemed characteristic of the accuracy of the PPE spectrometer in producing quantitative optical-to-thermal energy conversion efficiency spectra; they are clearly much smaller than the large spectral variations observed with the Ti:sapphire crystals.

To calculate $\eta_{NR}^{(b)}(\lambda)$ spectra for our samples the pairwise common values of $\beta_b(\lambda)$ and $A_s(\lambda)$ were inserted in the normalized equation for the PPE signal [Ref. 12, Eq. (19)]. The thermophysical values used in these calculations were[11] $\alpha_s=0.106$ cm^2/s; $k_g=2.38\times10^{-4}$ W cm^{-1} K^{-1}; and $\alpha_g=0.19$ cm^2/s. These values yielded $\gamma_{gs}=0.9989$. Similarly we used[10] $\gamma_{gp}=0.981$. Given that radiative emission from electronic states at the polished crystal surfaces is highly unlikely, we assumed that the value of the nonradiative energy conversion efficiency of those damaged layers was 1(=100%). In practice, it was found that the actual value of the surface-related $\eta_{NR}(\lambda)$ had little effect on the calculated values of $\eta_{NR}^{(b)}(\lambda)$. Figure 3 shows the $\eta_{NR}^{(b)}(\lambda)$ spectra for the two pairs of crystals, FOM=40, and FOM=800. These same spectra were also presented in Fig. 1 for direct correlations with optical-absorption spectra. Curves computed from Q-PPES data obtained from thick and thin crystals are shown for each pair. The deconvolution of surface and bulk processes produced values of $\eta_{NR}^{(b)}(\lambda)$ quite close to each other. The nonradiative efficiencies of each pair of samples increase for $\lambda>490$ nm. The FOM=40 curve attains the ~100% level above 640 nm, and then remains essentially flat. This spectral range coincides with the approximately equal competition between surface and bulk absorption modes, in the FOM=40 spectra.[12] This rapid near- and subthreshold rise of $\eta_{NR}^{(b)}(\lambda)$ can thus be attributed to residual absorptions in the crystal which are not related to the Ti^{3+} electronic optical transition manifold, but they are very likely due to bulk, purely nonradiative defects. The steeper increase of the $\eta_{NR}^{(b)}(\lambda)$ spectra corresponding to the FOM=800 pair of crystals ("annealed") for $\lambda\geq600$ nm is unbounded at 100% and, therefore, unphysical. The cause of this anomaly is the fact that $\beta_b(\lambda)$ plunges to zero in that wavelength range. Therefore, the computation raised the value of $\eta_{NR}^{(b)}(\lambda)$ to extremely high

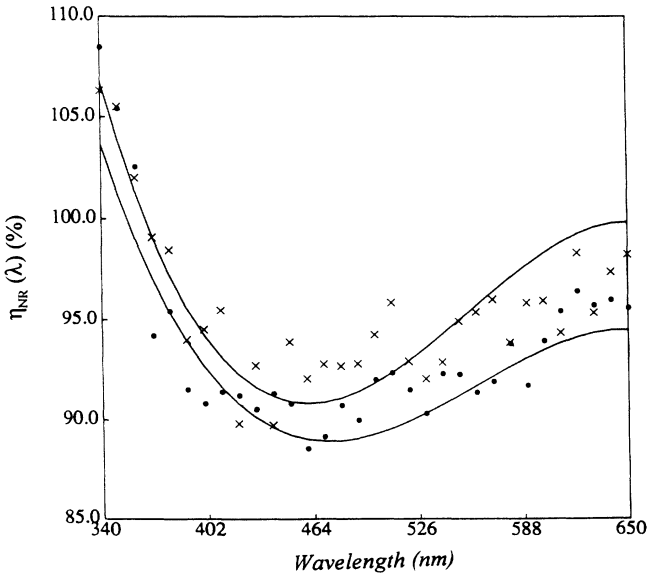

FIG. 2. Optical-to-thermal energy conversion efficiency spectrum of a sooted Si wafer using normalized quadrature (Q)-PPES. Data points were obtained using two successive experiments (to check reproducibility) in the 340–650-nm range to check spectral constancy and deviation from the theoretical 100% level. The curves are fourth-order polynominal fits to each set of data.

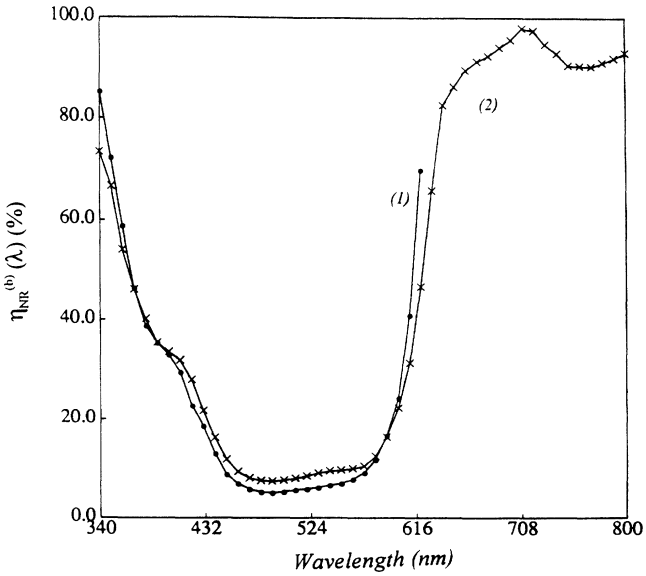

FIG. 3. Optical-to-thermal energy conversion efficiency spectra of the two pairs of Ti^{3+}:Al_2O_3 crystals. FOM=800 samples, Curve (1); FOM=40 samples, Curve (2). Each curve was generated from combined Q-PPES data and IP-PPES-determined β_b and A_s spectra from a pair of unequal length FOM crystals.

magnitudes, so that the value of the Q-PPE signal would remain finite and well behaved. Nevertheless, very good agreement exists in the $\lambda < 600$-nm range of the $\eta_{NR}^{(b)}(\lambda)$ curves of Fig. 3, which strongly indicates similar energy conversion mechanisms in the crystal bulk. This fact is expected, since the electronic $^2E_g \rightarrow {}^2T_{2g}$ transition normally dominates the optical spectrum of both crystals. The slightly higher $\eta_{NR}^{(b)}$ for the FOM=40 crystal pair is also expected, since the higher density of bulk nonradiative defect centers in these crystals is capable of inducing enhancement of the nonradiative transition quantum efficiency W_{NR} from the metastable excited state. The effect of this $\eta_{NR}^{(b)} \rightarrow W_{NR}$ increase resulted in visibly lower luminescence of the FOM=40 samples and is expected to produce laser rods with higher lasing threshold pump power. The following discussion aims to put on a theoretical footing several aspects of the nonradiative spectra presented in Fig. 3.

III. PHENOMENOLOGY OF Ti^{3+}:Al_2O_3 QUANTUM YIELD

The Ti^{3+} ion is a relatively simple two-state system in which the absorbed energy can be released either by emission of photons or by emission of heat. Therefore one can easily relate the nonradiative energy conversion efficiency $\eta_{NR}(\lambda, T)$ to the quantum efficiency of the system, $\eta_R(\lambda, T)$.

Defining η_{NR} as the fraction of the absorbed energy which is converted into heat, i.e., the optical-to-thermal (nonradiative) energy conversion efficiency, $\eta_{NR}^{(e)}$, one obtains[16]

$$\eta_{NR}^{(e)}(\lambda, T) = 1 - \eta_R(\lambda, T) \left[\frac{\lambda}{\lambda_e} \right] , \tag{3a}$$

where λ and λ_e are the absorption and peak emission photon wavelengths, respectively.

One can also define the nonradiative energy conversion quantum efficiency $\eta_{NR}^{(q)}$, which is related to the quantum yield as follows:

$$\eta_{NR}^{(q)}(\lambda, T) = 1 - \eta_R(\lambda, T) . \tag{3b}$$

Here $\eta_{NR}^{(q)}(\lambda, T)$ is defined as a probability that the excited system relaxes without radiative transitions.

In Eqs. (3a) and (3b) we have assumed that both $\eta_{NR}(\lambda, T)$ and $\eta_R(\lambda, T)$ depend on the photon wavelength λ and the temperature T. Relations (3a) and (3b) are essential for the analysis of the experimental data presented in Sec. II of this paper. Since it is easier to calculate theoretically the quantum yield than the nonradiative energy conversion efficiency, (experimentally, the opposite is true by virtue of photopyroelectric spectroscopy), we will compare the theoretical results with the experimental quantum yield indirectly obtained from PPES via the $\eta_{NR}^{(b)}(\lambda)$ spectrum using Eq. (3b). This equation is the more appropriate of the two equations (3a) and (3b), because PPES being a thermal energy detection technique, i.e., (number of photons)$\times$(energy/photon), it senses signals proportional to the incident photon energy. This implies that the λ dependence is automatically incorporated into the spectra of Fig. 3 and therefore the η_{NR} value need not be corrected with respect to the photon energy as in Eq. (3a).

IV. SIMPLE THEORY OF THE QUANTUM YIELD, IN A TWO-LEVEL SYSTEM

A. Kinetics of radiative and nonradiative deexcitation

In this section we consider the deexcitation process of an optically excited two-electronic-manifold system as preliminary toward the full treatment of the Ti^{3+}:Al_2O_3 system presented in Sec. V below. The basic assumption is that the system is excited by absorption of a photon and subsequently it loses its energy by emission of photons and phonons via radiative and nonradiative processes, respectively. The nonradiative intercenter energy transfer and additional excited-state absorption are negligible. We have described the energetic structure of this system using a simplified configuration coordinate diagram, where the ionic motion is considered in one-dimensional configuration space Q. Thus the excited- (e) and ground- (g) electronic manifolds are represented by two parabolas displaced due to the electron-lattice coupling (see Fig. 4). It should be mentioned that the one-dimensional diagram presented in Fig. 4, does not describe the real vibronic structure of the excited ^2E state in Ti^{3+}. Nevertheless this simplification is very useful because it allows the investigation of the dependence of the quantum efficiency of the system on the electron-lattice coupling strength without considering details related to the Jahn-Teller effect.

Without losing generality, each vibronic state $|\nu, n\rangle$ can be defined by the energy E_ν^n, and the appropriate state wave functions given, in the diabatic approximation, as follows:[4]

$$\phi_\nu^n(q, Q) = \phi_\nu(q) \chi_\nu^n(Q) , \tag{4}$$

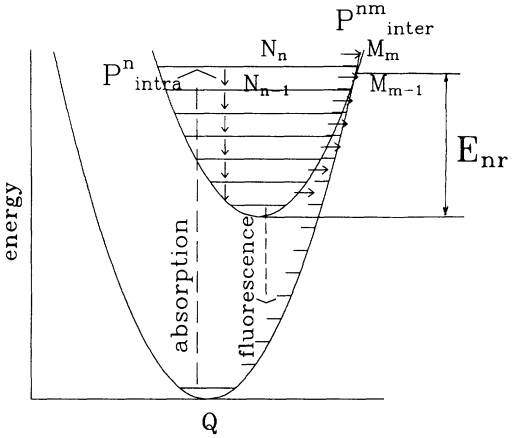

FIG. 4. Configurational coordinate diagram and vibronic structure of a two-electronic-manifold system. Radiative transitions are indicated by dashed arrows; nonradiative processes are indicated by solid arrows. The classical barrier for nonradiative transitions, i.e., the crossover energy E_{nr} is indicated in the figure.

where q is the electronic coordinate, ν is the quantum number of a given electronic manifold (e or g), and n is the vibronic quantum number. ϕ and χ represent the electronic and the vibronic parts of the total wave function, respectively. We have assumed that emission of photons takes place when the system is thermalized in the excited state, whereas nonradiative transitions can occur from an arbitrary excited state "before" and "after" the foregoing thermalization: One distinguishes fast processes, which take place "before" the system reaches thermal equilibrium in the first excited state and slow processes which take place "after" thermal equilibration. The fast nonradiative processes are intraconfigurational transitions during which the system relaxes, step by step, from $|\nu,n\rangle$ to $|\nu,n-1\rangle$ by emission of a phonon, with probability $P(\nu)^n_{\text{intra}}$; and interconfigurational nonradiative internal conversion, of probability $P(\nu\rightarrow\mu)^{nm}_{\text{inter}}$, where the system changes electronic and vibrational states from $|\nu,n\rangle$ to $|\mu,m\rangle$ without changing its energy ($E^n_\nu = E^m_\mu$). Due to these processes the system may either reach thermal equilibrium, while still in the excited metastable state, or it may relax all the way to the ground state. In the former case, further relaxation, by means of a radiative or nonradiative transition, is much slower. Characteristic time constants of these transitions are orders of magnitude larger than the fast nonradiative processes, and are usually determined by the radiative decay time.

Assuming that the initial state $|e,n\rangle$ is populated by steady-state excitation, one obtains the kinetics of deexcitation given by the following set of coupled equations (see Fig. 4):

$$\beta(\hbar\Omega)I_{\text{ex}}(\hbar\Omega)=[(N_n-M_m)P(e\rightarrow g)^{nm}_{\text{inter}} + N_nP(e)^n_{\text{intra}}]\hbar\Omega \ , \tag{5a}$$

$$0=(M_m-N_n)P(g\rightarrow e)^{mn}_{\text{inter}}+M_mP(g)^m_{\text{intra}} \ , \tag{5b}$$

$$N_nP(e)^n_{\text{intra}}=(N_{n-1}-M_{m-1})P(e\rightarrow g)^{n-1m-1}_{\text{inter}} + N_{n-1}P(e)^{n-1}_{\text{intra}} \ , \tag{5c}$$

$$M_{mP}(g)^m_{\text{intra}}=(M_{m-1}-N_{n-1})P(g\rightarrow e)^{m-1n-1}_{\text{inter}} + M_{n-1}P(e)^{m-1}_{\text{intra}} \tag{5d}$$

$$\vdots$$

$$N_{t+1}P(e)^{t+1}_{\text{intra}}=N_{tP^i_{\text{nr}}}-M_kP(e\rightarrow g)^{kt}_{\text{inter}}+N_tP^t_{\text{rad}} \ , \tag{5e}$$

$$M_{k+1}P(g)^{k+1}_{\text{inter}}=M_kP(g\rightarrow e)^{kt}_{\text{inter}}-N_tP_{\text{nr}} + M_kP(g)^k_{\text{intra}} \ . \tag{5f}$$

Interconfigurational transitions occur under the condition $E^i_e = E^j_g$ for any (i) and (j). In Equation (5a), $\beta(\hbar\Omega)$ is the absorption coefficient, $I_{\text{ex}}(\hbar\Omega)$ is the exciting photon irradiance, and N_i and M_j are the occupation numbers of the ith vibronic state related to the excited-electronic manifold and the jth vibronic state related to the ground-electronic manifold, respectively. The probabilities of internal conversion processes satisfy the relations

$$P(e\rightarrow g)^{ij}_{\text{inter}}=P(g\rightarrow e)^{ji}_{\text{inter}}\equiv P^{ij}_{\text{inter}} \ .$$

$P(g)^j_{\text{intra}}$ and $P(e)^i_{\text{intra}}$ are the probabilities for intraconfigurational nonradiative transitions inside the ground- and excited-electronic manifolds, respectively. N_t is the occupation number of the thermalized excited system; P^t_{rad} and P^t_{nr} are the radiative and nonradiative transition probabilities describing the deexcitation of the thermalized system.

To obtain the number of photons emitted per unit time, $N_{\text{phot}}=N_tP^t_{\text{rad}}$, one calculates N_t, using Eqs. (5). In general N_t can be calculated by the recurrence formulas

$$N_{s-1}=\frac{N_sP(e)^s_{\text{intra}}\Delta_{u-1}+M_uP(g)^u_{\text{intra}}P^{s-1u-1}_{\text{inter}}}{\Delta_{u-1}\Delta_{s-1}-(P^{s-1u-1}_{\text{inter}})^2} \ , \tag{6}$$

$$M_{u-1}=\frac{M_uP(g)^u_{\text{intra}}\Delta_{s-1}+N_sP(e)^s_{\text{intra}}P^{s-1u-1}_{\text{inter}}}{\Delta_{u-1}\Delta_{s-1}-(P^{s-1u-1}_{\text{inter}})^2} \ , \tag{7}$$

where

$$\Delta_{s-1}\equiv P^{s-1u-1}_{\text{inter}}+P(e)^{s-1}_{\text{intra}} \ , \tag{8}$$

$$\Delta_{u-1}\equiv P^{s-1u-1}_{\text{inter}}+P(g)^{u-1}_{\text{intra}} \ , \tag{9}$$

and the initial values of the N_n and M_m are given by

$$N_n=\frac{I_{\text{ex}}(\hbar\Omega)\beta(\hbar\Omega)\Delta_m}{[\Delta_m\Delta_n+(P^{nm}_{\text{inter}})^2]\hbar\Omega} \tag{10}$$

and

$$M_m=\frac{I_{\text{ex}}(\hbar\Omega)\beta(\hbar\Omega)P^{nm}_{\text{intra}}}{[\Delta_m\Delta_n+(P^{nm}_{\text{inter}})^2]\hbar\Omega} \ . \tag{11}$$

Usually intraconfigurational transitions are much more probable than interconfigurational ones. Therefore, one may assume that $N_i \gg M_j$, for any i and j and thus obtain

$$\hbar\Omega N_{\text{phot}}(\hbar\Omega)=I_{\text{ex}}(\hbar\Omega)\beta(\hbar\Omega) \times\left[\prod_{k=1}^{n(\hbar\Omega)}\frac{P(e)^k_{\text{intra}}}{P^{kl}_{\text{inter}}+P(e)^k_{\text{intra}}}\right] \times\frac{P^t_{\text{rad}}}{P^t_{\text{rad}}+P^t_{\text{nr}}(T)} \ . \tag{12}$$

Here l corresponds to the vibronic quantum number of the vibronic state related to the ground-electronic manifold, having the same energy as the k state of the excited-electronic manifold. Dividing Eq. (12) by $I_{\text{ex}}(\hbar\Omega)\beta(\hbar\Omega)$ one obtains the quantum yield of the system,

$$\eta_{\text{R}}[\hbar\Omega(\lambda),T]=\eta^n_{\text{R}}[\hbar\Omega(\lambda)]\eta^t_{\text{R}}(T) \ , \tag{13}$$

where

$$\eta^t_{\text{R}}\equiv\frac{P^t_{\text{rad}}}{P^t_{\text{rad}}+P^t_{\text{nr}}(T)} \tag{14}$$

is the quantum efficiency of the thermalized system, which generates the temperature dependence of η_{R} and

$$\eta_R^n \equiv \prod_{k=1}^{n(\hbar\Omega)} \frac{P(e)_{\text{intra}}^k}{P_{\text{inter}}^{kl}+P(e)_{\text{intra}}^k} \tag{15}$$

is the efficiency of the thermalization process which depends on the energy of the exciting photons. In Eqs. (12) and (14) we indicate explicitly the temperature dependence of the probability for nonradiative deexcitation of the thermalized system P_{nr}^t.

Equation (13) is of considerable significance. To appreciate its importance let us consider the relationship of the present model to what will be labeled "the standard approach," where the fast nonradiative internal conversion is not considered. Usually it is assumed that the intraconfigurational transitions are so fast that the depopulation of the highly excited vibronic states of the excited electronic manifold by internal conversion to the ground state is negligible. Hence assuming that radiationless transitions from the excited to the ground electronic manifold occur only after thermalization, one obtains a quantum yield which depends only on temperature. In our approach, this is equivalent to setting

$$\frac{P(e)_{\text{intra}}^k}{P_{\text{inter}}^{kl}+P(e)_{\text{intra}}^k}=1 \tag{16}$$

for any l and k, which yields from Eq. (15)

$$\eta_R^n=1 \ . \tag{17}$$

One of the purposes of this section is to show that condition (17) cannot be satisfied for systems with strong electron-lattice coupling, such as Ti^{3+}:Al_2O_3. Without detailed calculations it is actually easy to see that since η_R^n, Eq. (15), is given by the product of many factors, even if each factor differs little from unity, the resulting η_R^n can be significantly smaller than 1.

Considering that $\Omega=2\pi c\lambda^{-1}$, where c is the speed of light and λ is the exciting wavelength, it is easy to express the quantum yield as a function of λ. It should be noted here that the structure of Eq. (13) allows the calculation of the relative probability of the internal conversion process when the experimental dependence of η_R on λ is known. Using Eq. (13) one obtains

$$\frac{P(e)_{\text{inter}}^{n(\lambda)}}{P_{\text{intra}}^{nm}}=-\frac{\Omega_{\text{ph}}\lambda^2}{2\pi c}\eta_R^{-1}(d\eta_R/d\lambda) \ , \tag{18}$$

where Ω_{ph} is the phonon frequency.

B. Probability of nonradiative transitions and quantum efficiency

To calculate the probability of interconfigurational internal conversion, P_{inter}^{nm}, of an optically excited two-electronic-manifold system we have defined this quantity as a probability of transition induced by a time-independent perturbation H'. Thus[17]

$$P_{\text{inter}}^{nm}=\frac{2\pi}{\hbar}|T^{nm}|^2\rho(e)\delta(E_e^n-E_g^m) \ , \tag{19}$$

where $\rho(e)$ is the density of vibronic states related to the excited electronic manifold. Matrix elements T^{nm} depend on the nature of the Hamiltonian H'. When H' does not depend on the ionic coordinate Q one obtains[4]

$$T^{nm}=\langle\phi_e|H'|\phi_g\rangle F^{nm} \ , \tag{20}$$

where F^{nm} are the vibronic wave-function overlap integrals. It is useful to write the probability of internal conversion in the following form:

$$P_{\text{inter}}^{nm}=\tau_{\text{inter}}^{-1}|F^{nm}|^2 \ , \tag{21}$$

where the time constant τ_{inter} is related to the electronic matrix element $\langle\phi_e|H'|\phi_g\rangle$. For the purposes of the present generic system we have assumed $\tau_{\text{inter}}^{-1}=10^{14}\ \text{s}^{-1}$. In the next section, where the Ti^{3+} ion will be considered, we will use proper values for this and other parameters pertaining to that system.

The probability for nonradiative deexcitation of the thermalized system is related to probabilities of internal conversion as follows

$$P_{\text{nr}}^t(T)=\sum_n P_{\text{intra}}^{nm}B^n(T) \ , \tag{22}$$

where $B^n(T)$ is a Boltzmann occupation factor

$$B^n(T)=\frac{\exp[-(E_e^n-E_e^0)/kT]}{\sum_i \exp[-(E_e^i-E_e^0)/kT]\rho(E_e^i)} \ . \tag{23}$$

Since an operator for the annihilation of a local phonon is necessary for the intraconfigurational relaxation process, the probability of intraconfigurational nonradiative transition is proportional to the vibronic quantum number of the initial vibronic state:

$$P_{\text{intra}}^n=\tau_{\text{intra}}^{-1}n \ . \tag{24}$$

In Eq. (24), τ_{intra} is the characteristic time constant of the process. One can see that the probability of intraconfigurational transition increases linearly with the vibronic quantum number n whereas any increase of P_{inter}^{nm} is determined by the respective vibronic overlap integrals. The latter increase very rapidly when the energies of the excited- and ground-electronic manifolds are degenerate (crossover of parabolas in Fig. 4).[4,18]

It should be mentioned here that Eq. (24) indicates that relaxation inside the ground-electronic manifold following internal conversion is much faster than relaxation inside the excited-electronic manifold. To see this, one notices that for the states with the same absolute energies, $E_e^i=E_g^j$, $P^i(e)_{\text{intra}}<P^j(g)_{\text{intra}}$, since $j\gg i$. Thus $N_i>M_j$, even if $\tau(e)_{\text{intra}}$ is equal to, or comparable with, $\tau(g)_{\text{intra}}$.

To illustrate the competition between the inter- and intraconfigurational relaxation we have performed calculations of quantum yield vs the exciting photon wavelength. Although these calculations are not related to any real system, the simple one-dimensional configuration coordinate model used here makes the calculations easy enough, so as to draw some general conclusions concerning the importance of fast internal conversion processes. In the next section detailed calculations for the Ti^{3+} system, performed using a realistic vibronic structure, will be presented.

We have defined the energetic structure of the system by the energy of the zero-phonon transition ΔE and the phonon energy $\hbar\Omega$ which, in all cases, have been taken to be equal to 16 200 and 400 cm^{-1}, respectively. The electron-phonon coupling has been defined by the Huang-Rhys parameter S or by the displacement of the minima of energies in the configurational coordinate diagram $\Delta Q=(2S)^{1/2}$. In one-dimensional configurational space it is easy to calculate the crossover energy between the ground- and excited-electronic manifolds, E_{nr}. Assuming that $S\hbar\Omega<\Delta E$ one obtains,

$$E_{nr}=\hbar\Omega[(\Delta E/\hbar\Omega-S)^2/4S] . \quad (25)$$

In Table I we present the values of parameters describing the energetic structure of three possible two-level systems, *a*, *b*, and *c* used for illustration purposes. For these systems we have performed calculations of P^{ij}_{inter} vs the energy of the initial state and of the quantum yield η_R vs the wavelength. To calculate the overlap vibronic integrals we have used the Manneback recurrence formulas.[19] The probabilities for radiative deexcitation of the system have been assumed to be $P^t_r=\tau_r^{-1}=0.26\times10^6$ s^{-1}, which gives the radiative decay time $\tau_r=3.85$ μs.[6] Calculations have been performed for two values of the intraconfigurational decay constant: $\tau_{intra}=10^{-11}$ and 10^{-12} s.

The results of the calculations are presented in Figs. 5 and 6. In Fig. 5 the probabilities of inter- and intraconfigurational transitions vs energy of the initial vibronic state are presented, calculated with respect to the minimum energy of the excited-electronic manifold. The probability of intraconfigurational relaxation is indicated by dashed lines; curves I and II correspond to time constants τ_{intra} equal to 10^{-12} and 10^{-11} s, respectively. Curves *a*, *b*, and *c* correspond to internal conversion transition probabilities calculated for the model systems *a*, *b*, and *c*, respectively (see Table I). It can be seen that the probability of internal conversion increases rapidly with energy and reaches the maximum for a value slightly above the crossover of the parabolas E_{nr}. This maximum is determined by the maximum of the square of the vibronic wave-function overlap integral, which is of the order of $3-4\times10^{-2}$ at the maximum, and is almost independent of the electron-lattice coupling parameter.

Using Eq. (13) we have also calculated the quantum yields of the systems described by the parameters listed in Table I. The results are presented in Fig. 6. Calculations were performed for two temperatures $T=10$ and 320 K, and for two values of $\tau_{intra}=10^{-11}$ s (dashed curves) and 10^{-12} s (solid curves). The dotted lines represent the so-

TABLE I. Parameters of the energetic structure of three model systems. λ_{nr} corresponds to the wavelength of photons exciting the system just above E_{nr}.

Illustration system	S $\hbar\Omega=400$ cm^{-1}	E_{nr} (cm^{-1})	λ_{nr} (nm)
(a)	10	9303	392
(b)	11.25	7605	420
(c)	12	6769	435

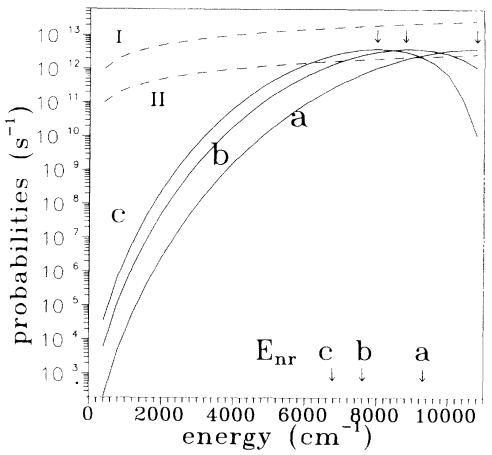

FIG. 5. Probabilities of the intraconfigurational and the internal conversion nonradiative processes vs energy of the initial vibronic state of several excited-electronic manifolds. The probabilities of intraconfigurational processes are presented by dashed lines. Curve I was obtained for $\tau^{-1}_{intra}=10^{12}$ s^{-1}; curve II was obtained for $\tau^{-1}_{intra}=10^{11}$ s^{-1}. The solid curves correspond to probabilities of internal conversion processes; *a*, *b*, and *c* correspond to model illustration systems characterized by the respective parameter sets in Table I. Crossover energies of the ground- and the excited-electronic manifolds F_{nr} as well as the maxima of P_{inter} are indicated by solid arrows.

called standard approach obtained using the *a priori* assumption $\eta^n_R=1$. For all the cases considered we have obtained significant decreases of the quantum yield for excitations above E_{nr}. In principle, the quantum yield will be related to the absorption spectrum of an electronic system. For medium strength electron-lattice coupling and when E_{nr} is large, the quantum yield remains constant at the absorption maximum. However, in cases where the system is strongly coupled to the lattice, E_{nr} is comparable to $S\hbar\Omega_{ph}$. As illustrated by case *c*, Table I, and Fig. 6(c), one can observe the quantum yield decreasing in the vicinity of the absorption maximum. Thus the quantum yield becomes smaller than unity, even at very low temperatures.

Using our model one can estimate the threshold ratio of the time constants: $(\tau_{inter}/\tau_{intra})$, for which the fast processes start to disturb the quantum efficiency of the system. In turns out that η^n_R is significantly smaller than unity when the probability of interconfigurational transitions is greater than 0.01 times the probability of intraconfigurational relaxation. For the values of the Huang-Rhys parameters listed in Table I, this gives the limiting value of τ_{inter}:

$$\tau_{inter}\cong0.1\tau_{intra} . \quad (26)$$

V. QUANTUM YIELD OF Ti^{3+} IN Al_2O_3

On applying the foregoing model to calculations of the quantum efficiency of Ti^{3+}:sapphire, one should take into account the specific energetic structure of this ion characterized by a large Jahn-Teller $E^*\epsilon$ effect in the ^2E state

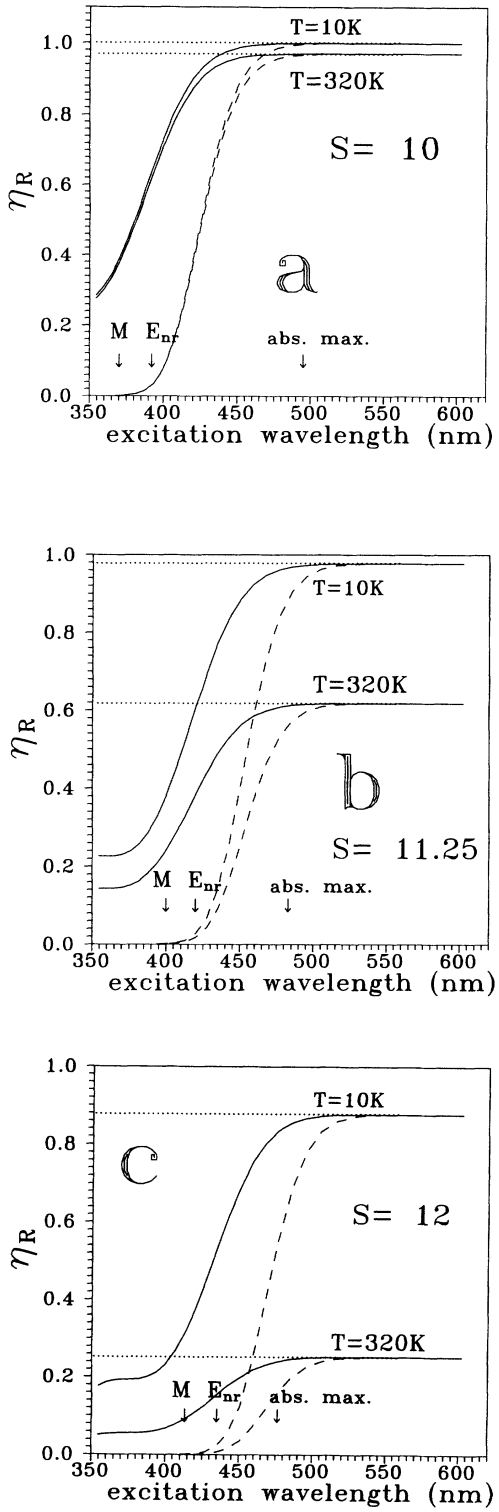

FIG. 6. Quantum yields vs wavelength of exciting photons. Solid curves correspond to $\tau_{intra}^{-1}=10^{12}\ s^{-1}$; dashed curves correspond to $\tau_{intra}^{-1}=10^{11}\ s^{-1}$; dotted lines correspond to the standard model, for which fast nonradiative internal conversion processes are negligible. (a), (b), and (c) correspond to the model systems described by parameter sets (a), (b), and (c), respectively, in Table I. In the figures the wavelengths corresponding to the probability maxima of internal conversion process are indicated by M; the crossover energies by E_{nr}; and the absorption maxima by "abs.max."

and a small Jahn-Teller $T^*\epsilon$ effect in the ground $^2T_2$ state. Moreover, the values of the system parameters, i.e., phonon energy and time constants related to the inter- and intra- non-radiative processes should be verified.

The energetic structure of the Ti^{3+} ion in sapphire has been extensively discussed in our earlier work.[4,20] We have found that there is a significant nonlinear electron-lattice coupling in this system in the excited state, and a small nonlinearity in the ground state. This effect causes the double phonon structure of the zero-phonon line in the absorption spectrum.[14,20] The resulting configurational coordinate diagram, obtained by analysis of the absorption and emission spectral lineshapes, is presented in Fig. 7. Here the section along the θ coordinate in a two-dimensional (θ,ε) configurational coordinate space is shown (the ε axis is perpendicular to the plane of the figure). Notice that the structure presented in Fig. 7 has a threefold rotational symmetry with respect to the point $\theta=0,\varepsilon=0$. Hence the energy of the excited electronic manifold has three equivalent minima and three saddle points. Parameters determining the diagram in Fig. 7 are listed in Table II.

Phonon structures observed in the emission as well as in the absorption spectrum,[2,14] allow the determination of the energies of local phonons related to the ground- and excited-electronic manifolds. Our calculations[20] based on the diagram presented in Fig. 7 yielded for the excited ^2E state two-phonon modes with energies 208 and 202 cm^{-1}. In the ground state the energy of both modes is approximately the same and is equal to 240 cm^{-1}, which is in full agreement with experiments.[14]

To obtain the quantum efficiency, $\eta_R^{Ti}(\lambda,T)$, of the Ti^{3+} we have calculated the nonradiative transition probability $P_{nr}^{t}(T)$ and the internal conversion probability $P(^2E\rightarrow{}^2T_2)_{inter}^{ij}$ according to Refs. 4 and 20, using a two-dimensional harmonic oscillator model to describe the vibronic structure of the ground- and excited-

TABLE II. Parameters of the configuration coordinate diagram and energetic structure of Ti^{3+} ion in sapphire used in this paper. The values of all parameters are the same as in Ref. 4 except for the nonlinearity in the $^2T_2$ state. Here we have used -0.055 instead of -0.043. Therefore, we have increased the value of the classical energy barrier for nonradiative transition E_{nr} from 4500 to 5000 cm^{-1}, as required in order to fit the calculated quantum efficiency of the Ti^{3+} to the experimental data. Coefficients of nonlinearity are given in units of Ω_{ph}/M, where Ω_{ph} is the phonon frequency and M is the reduced mass of the ions involved.

Ti^{3+}:Al_2O_3 electronic state	Jahn-Teller energy (cm^{-1})	Nonlinearity	Phonon energies E_{nr} (cm^{-1})	(cm^{-1})
$^2T_2$	132	−0.055	~240	
^2E	2924	0.236	208	
			202	
				~5000

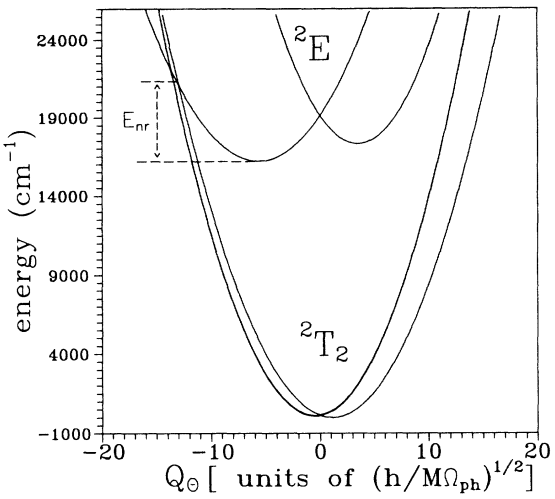

FIG. 7. Configuration coordinate diagram of octahedrally coordinated Ti^{3+} ion, corresponding to a cross section along the θ coordinate (see text). The diagrams were obtained using zero-phonon line energy equal to 16 200 cm^{-1}.

electronic-state manifolds:

$$P^t_{nr}(T)=\tau_0^{-1}\sum_n\sum_{k'=0}^{m}\sum_{k=0}^{n}\delta(E^n_{^2g}-E^m_{^2T_2})\times|F^{n-k\,m-k'}_{^2E^2T_2}|^2_{\parallel}|F^{kk'}_{^2E^2T_2}|_{\perp}B^n(T)\,, \tag{27}$$

and

$$P(^2E\rightarrow{}^2T_2)^{nm}_{inter}=\tau_0^{-1}\sum_{k'=0}^{m}\sum_{k=0}^{n}\delta(E^n_{^2E}-E^m_{^2T_2})\times|F^{n-k\,m-k'}_{^2E^2T_2}|^2_{\parallel}|F^{kk'}_{^2E^2T_2}|^2_{\perp}\,. \tag{28}$$

In the case of the Ti^{3+} ion, nonradiative transitions between the ^2E and $^2T_2$ electronic manifolds are allowed by the spin-orbit interaction[4,20] which mixes the electronic wave functions of the ^2E and $^2T_2$ states. Thus, the internal conversion time constant can be calculated as follows:

$$\tau^{-1}_{inter}=(2\pi/\hbar)\xi^2/\hbar\Omega_{ph}\,, \tag{29}$$

where $\hbar\Omega_{ph}$ is the phonon energy, $B^n(T)$ is the Boltzmann occupation factor, $|F^{n-k\,m-k'}_{^2E^2T_2}|_{\parallel}$ and $|F^{kk'}_{^2E^2T_2}|_{\perp}$ are the absolute values of the overlap integrals of the one-dimensional harmonic oscillator wave functions related to the parallel and perpendicular modes, respectively. In our case, subscripts "$\perp$ perpendicular" and "$\parallel$ parallel" correspond to the modes perpendicular and parallel to the plane of Fig. 7, respectively, (for details see Refs. 4 and 20).

Analysis of the vibronic structure of the excited state allows the determination of the spin-orbit matrix element ξ. In the case of Ti:sapphire ξ is equal to 80 cm^{-1}.[4] Equation (28) results in $\tau^{-1}_{inter}=3\times10^{13}$ s^{-1}.[4,20] The probability of the radiative transition has been assumed to be equal to 0.26×10^6 s^{-1}, i.e., the inverse of the radiative decay time of Ti^{3+}:sapphire at zero temperature. We have assumed that $P(^2E)^k_{intra}$ is given by Eq. (24) and we treated τ_{intra} as a free parameter of the model. Calculations have been performed using τ^{-1}_{intra} equal to 10^{13}, 10^{12}, and 10^{11} s^{-1}. The results are presented in Fig. 8. Figure 8(a) shows the inter- and intraconfigurational transition probabilities as functions of energy. Similarly to the case of one-dimensional configuration space a rapid increase of the probability of the internal conversion process is observed. This increase is even more rapid than in Fig. 5 because nonlinear coupling causes the increase of vibron-

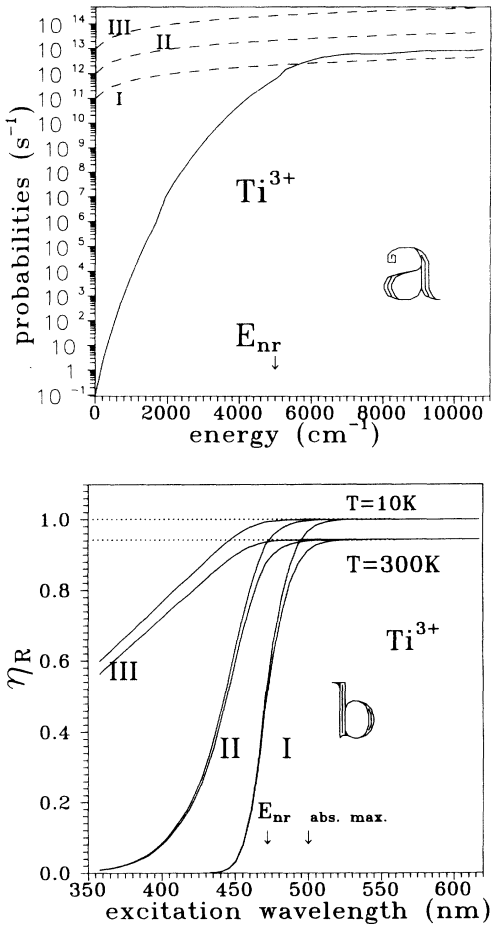

FIG. 8. (a) Probabilities of the intraconfigurational and internal conversion nonradiative processes as functions of energy of the initial vibronic state of the excited-electronic manifold in the Ti^{3+} system. The probabilities of intraconfigurational processes are represented by dashed curves. Curve (I): obtained using $\tau^{-1}_{intra}=10^{11}$ s^{-1}; Curve (II): obtained using $\tau^{-1}_{intra}=10^{12}$ s^{-1}; and curve (III): obtained using $\tau^{-1}_{intra}=10^{13}$ s^{-1}. The solid curve describes the probability of internal conversion process. (b) Quantum yield of the Ti^{3+} system vs wavelength of exciting photons. Solid curves correspond to η_R. Curves labeled (I): obtained using $\tau^{-1}_{intra}=10^{11}$ s^{-1}; Curves labeled (II): obtained using $\tau^{-1}_{intra}=10^{12}$ s^{-1}; and curves labeled (III): obtained using $\tau^{-1}_{intra}=10^{13}$ s^{-1}. Dotted lines correspond to the standard model for which fast nonradiative internal conversion processes are not considered. The wavelengths corresponding to excitation just above crossover energy E_{nr} and the absorption maximum are indicated with arrows.

ic wave-function overlap integrals for energies of the initial state much smaller than those for linear coupling. Nevertheless, the absolute values of probabilities for internal conversion are smaller than in the previous case as the result of the longer time constant τ_{inter}. The overall result is that the quantum yield starts to decrease for excitation energies greater than E_{nr}, Fig. 8(b). As shown clearly in that figure, the theory predicts that η_R^{Ti} starts to decrease for excitation wavelengths λ smaller than $\lambda_{nr}=480$ nm, with a slope which depends on the value of τ_{intra}.

VI. CALCULATION OF QUANTUM YIELD OF Ti^{3+} IN SAPPHIRE FROM PPES-DERIVED $\eta_{NR}^{(b)}(\lambda)$.

Using the theory of Sec. V and Eq. (3b), along with the PPES-derived nonradiative energy conversion efficiency $\eta_{NR}^{(b)}$, one can now reconstruct the experimental quantum-yield spectrum of the Ti^{3+}:Al_2O_3 system. We focus our attention in the spectral range 340 nm $<\lambda<620$ nm, where bulk absorption is dominant, Fig. 1. For optical excitation wavelengths above 620 nm and below 340 nm the measured η_{NR} is not related to the Ti^{3+} ions, as discussed in Sec. II B. Furthermore, weak bulk absorption can generate significant experimental errors in the value of $\eta_{NR}^{(b)}$, as discussed in the context of Fig. 3, curve (1). Figure 9 shows that the experimental quantum yield derived from the PPES quadrature spectrum, Eq. (3b), and the theoretical model developed in Sec. V is almost constant and equal to 90% for 450 nm $<\lambda<580$ nm. For λ smaller than 450 nm a significant

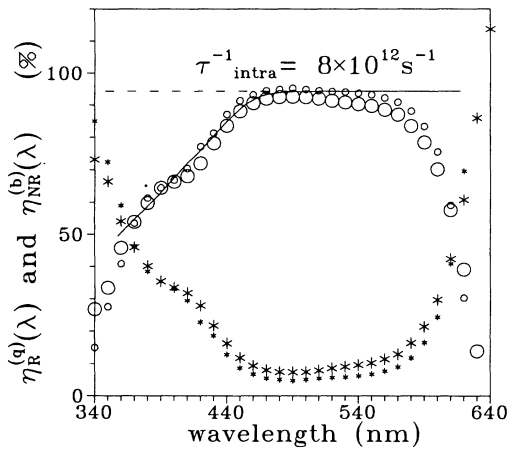

FIG. 9. Nonradiative and radiative transition efficiency spectra of FOM=40 and 800 crystal pairs of Ti^{3+}:Al_2O_3. Quantum yields $\eta_R(\lambda)$ are indicated by circles; nonradiative energy conversion efficiencies $\eta_{NR}^{(b)}(\lambda)$ are indicated by asterisks. Small (large) size symbols represent the FOM=(800) 40 crystal pair. The experimental quantum yields were obtained using PPE quadrature spectra in Figs. 1 and 3. The theoretical quantum yields calculated for $T=300$ K are represented by a solid line and were obtained using parameters listed in Table II, with the best-fit intraconfigurational relaxation time constant $\tau_{intra}=0.125\times10^{-12}$ s for both pairs of crystals. The dashed line corresponds to the standard model for which the internal conversion processes are negligible.

decrease of the quantum yield is observed. This effect is related to the increased probability of the internal conversion process in the Ti^{3+} ion excited to high vibronic states of the ^2E electronic manifold. Since the parameters of the configuration coordinate diagram and the phonon energies of the Ti^{3+} system were obtained from the PPES optical mode data, Fig. 1 and Refs. 4 and 20, the only free parameter used in our calculations was the intraconfiguration relaxation time constant τ_{intra}. The best fits to both crystal pairs with FOM=40 and 800 have been obtained for the $T=300$ K case using $\tau_{intra}^{-1}=8\times10^{12}$ s^{-1}. One should notice that for the range of λ where η_R is approximately constant, the theoretical quantum-yield spectrum is about 10% smaller than the experimental spectrum. This effect is most likely related to the inaccuracy of the estimation of the absolute $\eta_{NR}^{(b)}$ from the PPES signal, as indicated in the test Si wafer spectrum of Fig. 2. Another possible source of error may be the approximations used in the calculations of the theoretical $\eta_R(\lambda)$ spectrum. Specifically, it is possible that the vibronic wave-function overlap integrals have been overestimated, since we have used simple two-dimensional harmonic oscillator wave functions for describing the vibronic states related to the ^2E electronic manifold.

VII. CONCLUSIONS

In this work a complete theoretical and experimental spectral dependence of the bulk optical-to-thermal (nonradiative) and radiative quantum efficiencies of the Ti^{3+} ion in sapphire was presented. Unlike other approaches, the PPES methodology produces true bulk spectra, decoupled from (often substantial) crystal surface-induced nonradiative contributions. In setting up the appropriate two-dimensional theory for nonradiative transitions in Ti^{3+}:Al_2O_3, a precursor model was developed to investigate the influence of fast nonradiative internal conversion processes on the quantum efficiency of transition-metal ions. Conventionally, the internal conversion in unthermalized systems is assumed to be negligible, because the intraconfigurational relaxation is taken to be much more probable than nonradiative transitions which change the electronic state.

In dispensing with this *ad hoc* assumption, we obtained significant theoretical decrease of the quantum efficiency of the Ti^{3+} ion for exciting photon wavelengths smaller than 460 nm, corresponding to photon energy equal to 21 700 cm^{-1}. The quadrature PPE spectra of $\eta_{NR}^{(q)}(\lambda)$ strongly supported the foregoing theoretical prediction. These higher-than crossover E_{nr} energy photons populate the vibronic states of the ^2E electronic manifold. In this range of energies the probability of internal conversion was found to be quite large, thus decreasing the quantum efficiency. On the other hand, for excitation below E_{nr}, where the probability of internal conversion is small, the quantum yield of the system was found to be approximately constant. The experimental spectra from high- and low-FOM Ti:sapphire crystals were in good agreement with the theoretically predicted correlation between quantum efficiency of the Ti^{3+} system and the probability

for internal conversion. As a particular result of the fitting of the theory of the PPES data we have estimated the absolute value of the intraconfigurational relaxation time constant for the Ti^{3+} ion in the Al_2O_3 host.

Since it is well-known that without strong electron-lattice coupling internal conversion does not occur, another important generalized result of the successful theoretical fitting of the experimental $\eta_R(\lambda)$ spectrum is the conclusion that the intraconfigurational internal conversion processes are important for all systems strongly coupled to the lattice, and should not be neglected, a clear break from current theoretical practices.

ACKNOWLEDGMENT

The full support of this research by the Natural Sciences and Engineering Research Council of Canada (NSERC) through a Strategic Grant is gratefully acknowledged by both authors.

[1]S. Tanabe, Y. Sugano, and H. Kamimura, *Multiplets of Transition Metal Ions in Crystals* (Academic, New York, 1970).
[2]P. Albers, E. Stark, and G. Huber, J. Opt. Soc. Am. B **3**, 134 (1986).
[3]M. Yamaga, Y. Gao, F. Raheed, K. P. O'Donnell, B. Henderson, and B. Cockayne, Appl. Phys. B **51**, 329 (1990).
[4]M. Grinberg, A. Mandelis, and K. Fjeldsted, Phys. Rev. B **48**, 5935 (1993).
[5]C. E. Byvik and M. Buoncristiani, IEEE J. Quant. Electron. **QE-21**, 1619 (1985).
[6]P. F. Moulton, J. Opt. Soc. Am. B **3**, 125 (1986).
[7]F. Bantien, P. Albers, and G. Huber, J. Lumin. **36**, 363 (1987).
[8]M. J. Weber and L. A. Riseberg, J. Chem. Phys. **55**, 2023 (1971).
[9]M. Grinberg, A. Brenien, G. Boulon, C. Pedrini, C. Madej, and A. Suchocki, J. Phys. I (France) **3**, 1973 (1983).
[10]A. Mandelis and M. Zver, J. Appl. Phys. **57**, 4421 (1984).
[11]A. Mandelis, J. Vanniasinkam, S. Buddhudu, A. Othonos, and M. Kokta, Phys. Rev. B **48**, 6808 (1993).
[12]J. Vanniasinkam, A. Mandelis, S. Buddhudu, and M. Kokta, J. Appl. Phys. (to be published).
[13]P. Lacovara, L. Esterowitz, and M. Kokta, IEEE J. Quant. Electron. **QE-21**, 1614 (1985).
[14]B. F. Gachter and J. A. Koningstein, J. Chem. Phys. **60**, 2003 (1974).
[15]C. K. Jorgensen, Acta Chem. Scand. **11**, 73 (1957).
[16]J. Ramponi and J. A. Caird, J. Appl. Phys. **63**, 5476 (1988).
[17]A. S. Davydov, *Quantum Mechanics* (Nauka, Moscow, 1963).
[18]C. W. Struck and W. H. Fonger, J. Lumin. **10**, 1 (1975).
[19]C. Manneback, Physica XVII, 1001 (1951).
[20]M. Grinberg, A. Mandelis, K. Fjeldsted, and A. Othonos, Phys. Rev. B **48**, 5922 (1993).